

## DUST EXTINCTION AND MOLECULAR GAS IN THE DARK CLOUD IC 5146

CHARLES J. LADA AND ELIZABETH A. LADA

Harvard-Smithsonian Center for Astrophysics, 60 Garden Street, Cambridge, MA 02138

DAN P. CLEMENS

Department of Astronomy, Boston University, 725 Commonwealth Avenue, Boston, MA 02215

AND

JOHN BALLY

Department of Astronomy, University of Colorado, Boulder CO 80309

Received 1993 November 10; accepted 1994 January 14

### ABSTRACT

In this paper we describe a powerful method for mapping the distribution of dust through a molecular cloud using data obtained in large-scale, multiwavelength, infrared imaging surveys. This method combines direct measurements of near-infrared color excess and certain techniques of star counting to derive mean extinctions and map the dust column density distribution through a cloud at higher angular resolutions and greater optical depths than those achieved previously by optical star counting.

We report the initial results of the application of this method to a dark cloud complex near the cluster IC 5146, where we have performed coordinated, near-infrared, *JHK* imaging and  $^{13}\text{CO}$ ,  $\text{C}^{18}\text{O}$ , and CS millimeter-wave, molecular-line surveys of a large portion of the complex. More than 4000 stars were detected in our *JHK* survey of the cloud. Of these, all but about a dozen appear to be field stars not associated with the cloud. Star count maps at *J* band show a striking and detailed anticorrelation between the surface density of *J*-band sources and CO and CS molecular-line emission. We used the (*H*–*K*) colors and positions of nearly 1300 sources to directly measure and map the extinction and thus trace the dust column density through the cloud at an effective angular resolution of 1.5. We report an interesting correlation between the measured dispersion in our extinction determinations and the extinction. Modeling this relation indicates that effects of small-scale cloud structure dominate the uncertainties in our measurements. Moreover, we demonstrate that such observations can be used to place constraints on the nature of the spatial distribution of extinction on scales smaller than our resolution. In particular, we show that models in which the dust is distributed uniformly or in discrete high-extinction clumps on scales smaller than 1.5 are inconsistent with the observations.

We have derived extinctions at the same positions and at the same angular resolution (1.7) as our molecular-line observations. This enabled a direct comparison of  $^{13}\text{CO}$ ,  $\text{C}^{18}\text{O}$ , and CS integrated intensities and column densities with  $A_V$  for more than 500 positions in the cloud, corresponding to a range in  $A_V$  between 0–32 mag of extinction. We found the integrated intensities of  $^{13}\text{CO}$ ,  $\text{C}^{18}\text{O}$ , and CS to be roughly linearly correlated with extinction over different ranges of extinction. However, for all three molecules we find the scatter in the observed relations to be larger than can be accounted for by instrumental error, suggesting that there are large intrinsic variations in the abundances or excitation of the molecules through the cloud. Mean abundances for all the molecules relative to hydrogen were directly derived from the data. The ratio of  $^{13}\text{CO}$  to  $\text{C}^{18}\text{O}$  abundances was found to be significantly higher than the terrestrial ratio in regions where extinction is less than 10 mag. In the same region, the dispersion in the abundance ratio is also found to be very large, suggesting that the abundances of one or both molecules are very unstable even at relatively large cloud optical depths. Beyond 10 mag of extinction the abundances of both species appear very stable with their ratio close to the terrestrial value.

*Subject headings:* dust, extinction — ISM: abundances — ISM: individual (IC 5146) — ISM: molecules — techniques: photometric

### 1. INTRODUCTION

Molecular clouds in the galaxy are composed almost entirely of molecular hydrogen ( $\text{H}_2$ ). However, two factors render  $\text{H}_2$  generally unobservable in such clouds. First, because it is a homonuclear molecule,  $\text{H}_2$  lacks a permanent dipole moment, and its rotational transitions are extraordinarily weak. Second, being the lightest interstellar molecule, its lowest energy rotational transitions are at mid-infrared wavelengths, which are both inaccessible to observation from the earth and also too energetic to be collisionally excited at temperatures (i.e., 10 K) characteristic of cold molecular clouds.

Consequently, the most basic physical properties (e.g., size, mass, density, and temperature) of molecular clouds have been derived almost exclusively from observations of rare, trace molecules such as CO, CS, and  $\text{NH}_3$ , which are typically  $10^4$ – $10^9$  times less abundant than molecular hydrogen. Variation in chemical abundances, opacities, and excitation conditions complicate interpretation of the results derived from these molecular hydrogen surrogates.

In lieu of observing molecular hydrogen, the most direct way to trace the hydrogen content of a molecular cloud is to measure the distribution of dust through it. This is because of

the constancy of the gas-to-dust ratio in interstellar clouds, which has been observationally well established (e.g., Lilley 1955; Jenkins & Savage 1974; Bohlin, Savage, & Drake 1978). In principle, the overall distribution of dust in a cloud can be directly traced by measurements of the extinction of background starlight produced at visual and near-infrared wavelengths by the cloud. Historically, such measurements have been severely limited by the lack of sufficient numbers of background stars, which could be observed through the cloud. However, as we will demonstrate in this paper, the advent of sensitive near-infrared array cameras has dramatically altered this situation.

Traditionally, the general method to derive the extinction in a dark molecular cloud has been throughout use of star counts (Bok & Cordwell 1973). In this method a rectilinear grid is overlaid on a photographic image of a cloud, and the number of stars in each box or reseau square in the grid is counted. These counts are compared to counts in a nearby, unobscured, comparison field. With knowledge of the (apparent) luminosity function of field stars in the general direction of the cloud, the ratio of counts ON and OFF the cloud can be converted directly into an extinction. This technique suffers from a number of limitations (Rossano 1980), the principal one being the uncertainty introduced by Poisson statistics. This uncertainty is given by  $\sqrt{n}$ , where  $n$  is the number of stars counted in a reseau square (Bok 1937).

The most extensive star counting studies of molecular clouds have involved counts of stars on optical prints of the Palomar Observatory Sky Survey (e.g., Dickman 1978; Rossano 1978; Cernicharo & Bachiller 1984; Mattila 1986). Unfortunately, the dynamic range of such optical star counts is limited. For example, on an unobscured region of a POSS print in the Perseus region, there are typically  $10^4$  stars per square degree (Cernicharo & Bachiller 1984). However, on size scales of  $2''$ – $3''$ , comparable to those characteristic radio molecular-line observations, only about 25–35 stars are counted in regions with no extinction. Consequently, only 3.5–4 mag of visual extinction are sufficient to reduce the number of stars within a single reseau square to unity. Moreover, systematic uncertainties can dominate statistical uncertainties in such studies (Rossano 1980), rendering extinction estimates above about 3 visual mag highly uncertain. It would clearly be important to be able to determine extinctions in more opaque and denser regions of molecular clouds, where star formation occurs and molecules other than  $^{12}\text{CO}$  and  $^{13}\text{CO}$  are found.

Since extinction decreases with wavelength, observations made at longer wavelengths can detect more background stars through a cloud and probe deeper cloud depths (e.g., Dickman & Herbst 1990; Straw & Hyland 1989). For example, a star suffering 10 mag of visual extinction will be extinguished by 2.8 mag at  $J$  ( $1.25\ \mu\text{m}$ ) and only 1.1 mag at  $K$  ( $2.2\ \mu\text{m}$ ). With the development of large-format infrared imaging detectors, it is now possible to obtain infrared star counts which are capable of measuring dust column densities over relatively larger regions of the sky with a dynamic range 5–10 times larger than previous optical studies. More significantly, however, multi-channel array cameras make possible simultaneous, *multicolor* infrared surveys of molecular clouds. It has been long appreciated that infrared color excess can be used to *directly* determine extinction to individual stars behind molecular clouds (e.g., Jones, Hyland, & Bailey 1981; Frerking, Langer, & Wilson 1982). However, with single-channel infrared detectors, only small numbers of background stars could be practically

observed at more than one wavelength through any given molecular cloud. Consequently, such observations could not compete with star count studies for determining the distribution of extinction through a cloud or for comparison with molecular-line observations. Infrared array cameras largely remove this limitation by making it possible to simultaneously determine the colors of hundreds to thousands of background sources through a molecular cloud. This enables the implementation of a new and more direct technique for measuring and mapping extinction than star counting. This method, which we introduce and describe in this paper, uses measurements of infrared color excess together with certain aspects of star counting to directly derive and map the extinction through a cloud. Because infrared color excess is proportional to dust column density, the extinction maps produced by this method also accurately trace the distribution of dust through a cloud.

In this contribution, we report the initial results of the application of this method of extinction determination to the molecular cloud complex near IC 5146. IC 5146 is a young cluster in Cygnus. On optical photographs it appears associated with a large complex of dark clouds which extends more than  $2^\circ$  to its west. Overall, the cloud has a filamentary appearance and is morphologically similar to the famous  $\rho$  Ophiuchi cloud complex. Recently, Dobashi et al. (1992) obtained a large-scale  $^{12}\text{CO}$  survey of the complex which traced its complete extent. Dobashi et al. (1992) derived a mass of approximately  $4500\ M_\odot$  for this entire complex, which is slightly more massive than the well-known Taurus cloud complex.

We have performed an extensive and coordinated near-infrared imaging/molecular-line survey of a large portion of this dark cloud. From our infrared observations we obtained ( $H-K$ ) infrared colors of more than 1000 stars and used them to directly measure and map the extinction through the cloud at the same and higher angular resolutions as our molecular-line observations. This enabled both a very accurate determination of the cloud mass as well as direct measurements of the LTE abundances of  $^{13}\text{CO}$ ,  $\text{C}^{18}\text{O}$ , and CS between 0–30 mag of visual extinction, a range of extinction roughly 25 mag greater than that investigated in previous optical star count studies.

In § 2 we describe our data collection and reduction methods. Section 3 reports the basic results of these observations. In § 4 we describe our method for measuring infrared extinction and determining the distribution of extinction through the cloud. In § 5 we compare the extinction measurements with molecular line observations, evaluate and discuss the limitations and uncertainties in the method, and discuss the implications of our observations for understanding the structure of the molecular cloud. Section 6 presents a concise summary of our major results.

## 2. OBSERVATIONS AND DATA REDUCTION METHODS

### 2.1. Infrared Array Camera Observations

The near-infrared imaging data were obtained using the National Optical Astronomy Observatory (NOAO) Simultaneous Quad Infrared Imaging Device (SQUIID) on the Kitt Peak National Observatory (KPNO) 1.3 m telescope in 1991 September. SQUIID is equipped with four  $256 \times 256$  platinum silicide (PtSi) focal plane arrays. Dichroic mirrors were used to allow simultaneous observations at four infrared wavelength bands:  $J$  ( $1.2\ \mu\text{m}$ ),  $H$  ( $1.6\ \mu\text{m}$ ),  $K$  ( $2.2\ \mu\text{m}$ ), and  $L$  ( $3.4\ \mu\text{m}$ ). For

this experiment, we obtained data in the  $J$ ,  $H$ , and  $K$  bands. The optics were configured to provide a field of view of approximately  $5.9 \times 5.9$  and a resolution of  $1.39$  per pixel at  $J$  band. At  $K$  band the resolution was  $1.36$  per pixel. SQUID  $JHK$  images were obtained in three regions of the cloud complex. Twenty-four images were obtained at each wavelength band in a roughly  $5 \times 5$  mosaic grid centered on the optical cluster, IC 5146. An additional 24 SQUID fields were observed in a  $3 \times 8$  mosaic grid toward a portion of the dark cloud well removed from the cluster. Finally, four SQUID fields were observed at each band in a control region off the cluster and molecular cloud in an area apparently devoid of extinction and molecular emission. In this paper we will discuss the results obtained for the dark cloud region, which we designate as the Northern Streamer, and the four control fields. Observations of the cluster region will be presented elsewhere (Lada et al. 1994).

The fields observed in the direction of the Northern Streamer were spatially overlapped by  $\sim 0.9$  in both right ascension and declination, allowing for both the accurate positional placement of the mosaicked fields and redundancy of our photometric measurements of sources located in the overlapped regions. The control field images were not overlapped. The integration time in each filter, for observations both on and off IC 5146, was 3 minutes. Each ON field was observed twice, with a  $15''$  offset or dither between observations. A combination of the standard Image Reduction and Analysis Facility (IRAF) routines<sup>1</sup> and custom software were used for data reduction. The data were reduced by subtracting a dark frame from each image, dividing by a flat field, and then subtracting the value of the local sky. To construct flat fields, the median sky level for each subtracted image was determined and used to normalize each frame. Eight different flat fields for each filter were constructed by median filtering (to remove stars and extended emission) the 13 time-neighboring normalized images. These 24 (8 frames times 3 filters) flat-field images were also autonormalized before division into the appropriate dark-corrected (but not normalized) images.

Comparisons to the conventional sky removal method (direct, frame-by-frame sky subtraction) were performed to verify the quality of the images produced by our nonconventional method. Analysis of photometric values returned by both methods found virtually identical results for identified stars. However, our median-median method produced images with lower rms sky noise and a lack of the common negative-going defects produced by incomplete removal of extended stellar point-spread functions (PSFs) in the conventional method sky (reference) images. Because the sky brightness levels were significantly variable during the observing for this project, the initial normalization before median filtering enabled more complete removal of the stellar PSFs in the computed flat-field frames than occurred using the conventional approach.

Stellar profiles were examined for each image and showed full width at half-maximum (FWHM) intensities between  $1.5$  and  $2.1$ , with a mean of  $1.9$  and a dispersion of  $0.1$ . The routine DAOFIND was used to extract sources with a finding threshold set to 5 times the rms sky noise in each frame. Photometry was obtained for all extracted stars in the final images

using APPHOT for a number of different aperture sizes. Photometric measurements were independently obtained for each dithered pair of images toward each field. Custom stellar matching software was used to compare the magnitudes obtained for each dithered stellar pair. Plots of the difference magnitudes for each star versus the mean magnitude showed no systematic offset, while still displaying the flared errors at faint magnitudes expected. Further, plots of the difference magnitude versus the internal photometric uncertainties, returned by APPHOT, showed no unexpected effects or features. We conclude that the internal APPHOT uncertainties are reasonably good estimators of the true photometric uncertainties.

Histograms of the apparent magnitude distributions of stars which were identified and matched across the dithered pairs of frames were plotted along with histograms of the magnitudes for stars which were found in only one or the other frame. The latter showed a peak at faint magnitudes exactly coinciding with the faint edge (the faint magnitude half-power point) of the peak of the matched star distribution. The conclusion drawn was that *both* distributions are returning information concerning the completeness limit, in the form of the numbers of stars detected and missed as a function of apparent magnitude. Using these distributions together and moving to brighter magnitudes, where the fraction of missed stars falls to 10% or less, we estimate that our imaging and stellar photometric extractions are 90% complete in the individual dithered image pairs to  $m_J = 14.6$ ,  $m_H = 14.1$ , and  $m_K = 13.1$ . In order to extend the completeness another 0.75 mag fainter, each pair of dithered images was registered and added, and stars were refound and photometered, yielding totals of 5793, 5732, and 3184 stars in the  $J$ ,  $H$ , and  $K$  bands, respectively, for the 24 target and four reference fields.

The average number of stars found per frame was about 200 at  $J$ , reducing the need for PSF fitting photometric extractions. However, some stars were closely placed, requiring stopping down the synthetic stellar apertures to avoid contamination for these stars. In order to determine the run of stellar flux with aperture size, moderately bright, but well-isolated stars on each frame, and in each filter, were measured for all stellar apertures (from  $2.3$  to  $3.0$  radius) and for two very large apertures (up to  $5.5$  radius). All stellar magnitudes were thus scaled up to a uniform, large effective aperture.

Coordinates (epoch 2000) for stars found in the Northern Streamer (but not the reference fields) were established based on a combination of *Hubble Space Telescope* (*HST*) guide stars and stellar matches from neighboring infrared images. Two of the infrared fields, located on opposite right ascension ends of the  $8(\alpha) \times 3(\delta)$  mosaic, had three or more *HST* guide stars contained in them. Matching of these optical stars to their infrared counterparts established rough plate scales and instrument rotation angles, relative to the equatorial system. Frame center coordinates were determined and used to generate equatorial coordinates for infrared stars near the image boundaries which had corresponding matching infrared stars in neighboring frames. This coordinate passing technique was repeated from the initial mosaic frame (containing 5 *HST* guide stars) through nine neighboring frames to the check frame (containing three *HST* guide stars). In this fashion, the effective pixel resolution for coordinate determination is increased from about 100–200 (the largest pixel separation between *HST* stars on a single infrared image) to about 1500–1800 (separation across eight frames). Careful attention to proper projections (gnomic) and deprojections were included in the process. Plate

<sup>1</sup> IRAF is distributed by the National Optical Observatories, which are operated by the Association of Universities for Research in Astronomy (AURA), under cooperative agreement with the National Science Foundation.



scale and instrumentation angle parameters (in each filter) were fine-tuned and the matching repeated until the *HST*-to-infrared stellar positional match over nine frames of separation was perfect. Checks of the infrared-based on *HST* guide star coordinates for stars found between the two reference frames show rms offsets under  $0''.5$ . We estimate that the final coordinates of the infrared stars are accurate to  $0''.5$  or better, chiefly limited by the unknown astrometric quality (flatness and pixel uniformity) of the PtSi arrays used.

Provisional stellar magnitudes and colors (see below) were computed and examined for systematic effects. We found a significant tendency for stars imaged onto the outer 10% of the PtSi SQUID arrays to show unusual colors. This effect was discovered in plots of mean stellar colors ( $J-H$ ), ( $H-K$ ), and ( $J-K$ ) versus raw array  $X$  and versus  $Y$  coordinates of the stars. Two of these functions showed anomalous stellar colors which were redder or bluer than stars imaged in the central portions of the array. To remove this effect, stars imaged onto the outer 10% of the array had their corresponding photometry rejected. Coordinates were established for the remaining stars in all the target frames, and all surviving data were merged into one database for the target data and another for the reference data. Duplicate stars, from neighboring target frames (up to four), were identified and their magnitudes and positions refined by a rule-based averaging process, which accounted for imperfect sky coverage of the individual  $J$ ,  $H$ , and  $K$  SQUID arrays. Also, nonstellar entries (chiefly diffraction spikes) were identified and removed from the database.

Calibration sources were selected from the list of Elias et al. (1982) and were observed on the same nights and through similar air masses, as were observations of the target and reference images. Since the SQUID system is close to the Johnson system (e.g., Lada, Young, & Green 1993) we elected to use the SQUID camera filters and arrays as our standard system, and to use in-band observations of the standards to establish the filter zero points independently. Since the standard were observed at about the same airmasses, infrared extinctions are very small (0.1–0.2 magnitudes per airmass), and our reported magnitudes and colors are likely not in error by much more than their photometric uncertainties determined by APPHOT.

## 2.2. Millimeter-Wave, Molecular-Line Observations

We obtained observations of the 110 GHz  $J = 1-0$   $^{13}\text{CO}$ , the 109 GHz  $J = 1-0$   $\text{C}^{18}\text{O}$ , and the 98 GHz  $J = 2-1$  CS molecular emission lines toward the IC 5146 cloud complex during the period between approximately 1991 January to 1991 April. These observations were made using the AT&T Bell Laboratories 7m offset Cassegrain antenna, Located in Holmdel, New Jersey. This instrument had a very clean Gaussian beam with a FWHM of roughly  $100''$ , which was independent of frequency between 98 and 115 GHz. The primary beam efficiency was about 87% and the aperture efficiency (which is determined by the 14dB edge taper of the illumination pattern) about 55%. The detector was a liquid-helium-cooled SIS receiver built by NRAO with a single sideband temperature  $T_{\text{SSB}} \sim 75-130$  K. The observations were made by both in-band frequency-switching, in which the reference frequency is displaced from the signal by 6.4 MHz, as well as the multiple-mapping position-switching mode described by Bally et al. (1987). We used a 250 kHz filterbank with 256 channels, one-half of which were sent to a spectrum expander (Henry 1979) to give a resolution of 100 or 50 kHz ( $0.31 \text{ km s}^{-1}$  or  $0.15 \text{ km s}^{-1}$  at 98 GHz). Integration times were adjusted so that the

rms noise temperature in the 50 kHz channels was 0.5 K for the  $^{13}\text{CO}$  observations and 0.2 K for  $\text{C}^{18}\text{O}$  and CS observations. All data were calibrated with a blade chopper that permits rapid comparison between the sky and a 77 K liquid-nitrogen-cooled reference load or the 77 K load and an ambient temperature absorber. The receiver noise temperature and the temperature scale was determined by comparing a room temperature load to the liquid-nitrogen load. Then the sky brightness temperature was measured by comparison of the sky emission with the cold load. A simple atmospheric model was used to scale the observed intensities to the brightness temperature that would have been measured by this antenna above the atmosphere. The details of the receiver and calibration procedure have been described elsewhere (Pound, Bania, & Wilson 1990). All data were reduced using the COMB spectral line reduction package. Frequency-switched spectra were folded, and linear baselines were removed from the spectra. Baselines were fitted to that portion of the spectrum which is devoid of emission. Spectra were examined, and bad channels were eliminated.

## 3. RESULTS

### 3.1. Molecular-Line Observations

We first surveyed the complex in the  $^{13}\text{CO}$  line in a fast-mapping mode to determine the extent of the molecular emission. Subsequent observations in the  $\text{C}^{18}\text{O}$  and CS emission lines were confined to those regions where significant  $^{13}\text{CO}$  emission was detected. These latter observations were obtained with typically 2 to 3 times the integration time as the  $^{13}\text{CO}$  observations. Figure 1 shows the resulting maps of the integrated emission from the  $^{13}\text{CO}$  and CS.

The map of integrated  $^{13}\text{CO}$  emission (Fig. 1a) delineates the extent of the molecular emission from this dark cloud complex. The distribution and extent of the  $^{13}\text{CO}$  emission agrees well with that of the optical extinction observed on the POSS print of this region, as well as with the lower resolution  $^{12}\text{CO}$  and  $^{13}\text{CO}$  maps of this cloud obtained by Dobashi et al. (1992). Our  $^{13}\text{CO}$  map indicates that the complex consists of three major subunits: the cluster, the Northern Streamer, and the Southern Streamer. The cluster is located at the eastern end of the complex, and itself consists of three bright emission cores which were originally identified in the early  $^{12}\text{CO}$  observations of Lada & Elmegreen (1979). This region was designated as cloud E in the Dobashi et al. (1992) study and contains the brightest  $^{13}\text{CO}$  and  $^{12}\text{CO}$  emission in the complex. The second most prominent region is the Northern Streamer (cloud C in the Dobashi et al. nomenclature) which is located about  $1^\circ$  west and  $0.3^\circ$  north of the cluster region. The third most prominent region is the Southern Streamer (cloud B in the Dobashi et al. nomenclature) located about  $0.3^\circ$  south of the Southern Streamer.

Figure 1b shows the integrated intensity CS map. The same general features that are evident in this map as are also seen in the  $^{13}\text{CO}$  map. However, in detail the two maps are strikingly different. The strongest CS emission originates in the Northern Streamer and not the cluster, clearly indicating that the  $^{13}\text{CO}$  to CS intensity ratio varies strongly within the cloud. Emission from  $\text{C}^{18}\text{O}$  was mapped only around the cluster and in the Northern Streamer region. In these regions the distribution of  $\text{C}^{18}\text{O}$  emission is comparable to CS; in particular, like CS, the  $\text{C}^{18}\text{O}$  emission peaks in the Northern Streamer region rather than toward the cluster.

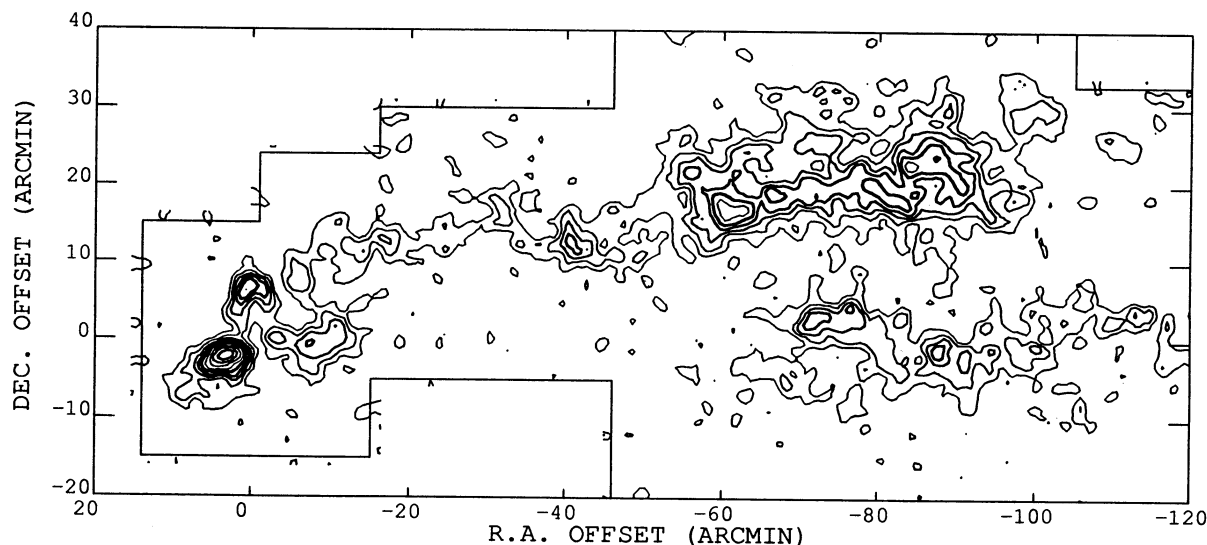


FIG. 1a

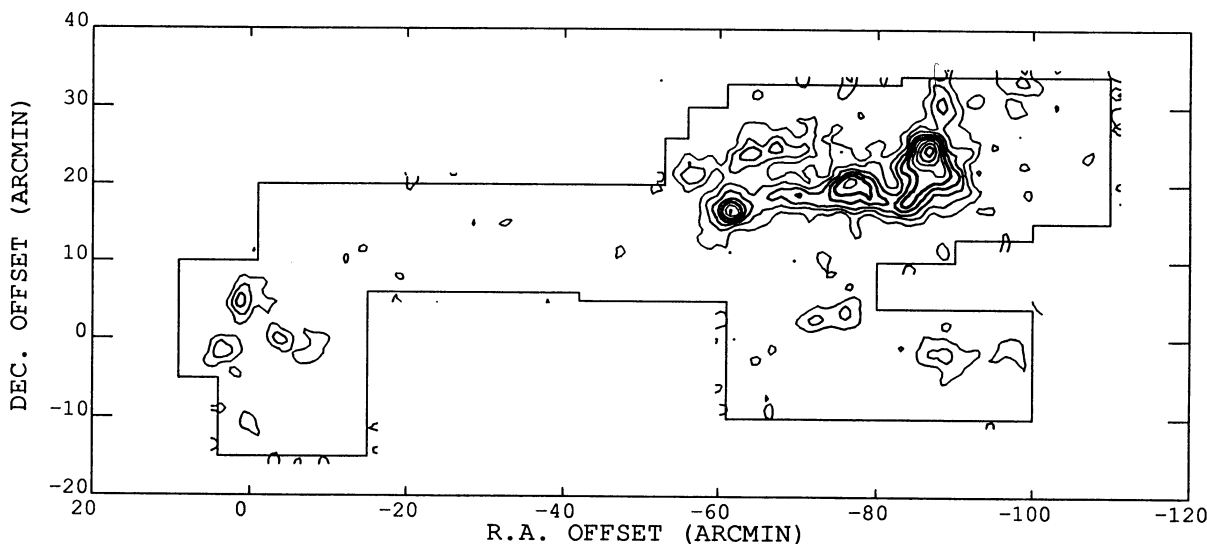


FIG. 1b

FIG. 1.—(a) The  $^{13}\text{CO}$  ( $J = 1 \rightarrow 0$ ) integrated intensity map ( $\Delta V = 2 - 10 \text{ km s}^{-1}$ ) of the IC 5146 complex made with the Bell Laboratory Telescope. The lowest contour is  $1.5 \text{ K km s}^{-1}$ . Subsequent contours increase in steps of  $1.5 \text{ K km s}^{-1}$ . The reference (0,0) position of the map is  $\alpha_{1950} = 21^{\text{h}}51^{\text{m}}54^{\text{s}}$ ;  $\delta_{1950} = +47^{\circ}01'12''$ . The cluster IC 5146 is located at the (0,0) position of this map. The Northern Streamer is the region of bright emission centered approximately at map coordinates  $(-80, 20)$ . (b) The integrated intensity map of CS emission in the IC 5146 region. The lowest contour plotted here is at  $0.2 \text{ K km s}^{-1}$ . Subsequent contours increase in equal steps of  $0.2 \text{ K km s}^{-1}$ . Otherwise the same as (a).

### 3.2. Infrared Imaging Observations

#### 3.2.1. Stellar Spatial Distribution

Figure 2 shows the positions of all the 3760  $J$ -band stars with  $J \leq 16$  mag that we extracted from the infrared images of the Northern Streamer region of the IC 5146 dark cloud complex. The surface density of  $J$ -band stars is relatively high but clearly not uniform across this region of the dark cloud. To obtain a more quantitative estimate of the distribution of stellar surface density, we constructed a star count map of the region from the observations shown in Figure 2. The star counts were obtained by subdividing the region into a rectangular grid of overlapping squares, each  $1.5 \times 1.5$  in size, and then counting the total number of stars in each square. The centers of each such resau square were separated by 0.75, the Nyquist spatial sampling interval. The number of stars counted in each

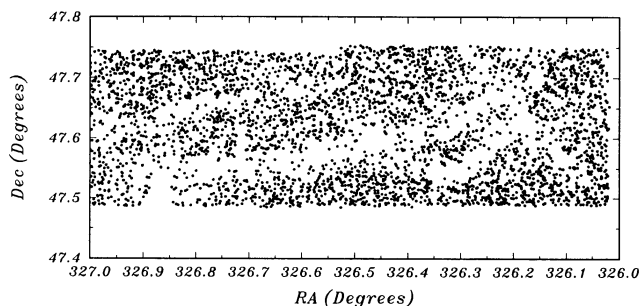


FIG. 2.—Map of the distribution of stellar positions of all  $J$ -band stars brighter than the completeness limit toward the Northern Streamer. The coordinate system is epoch 2000.

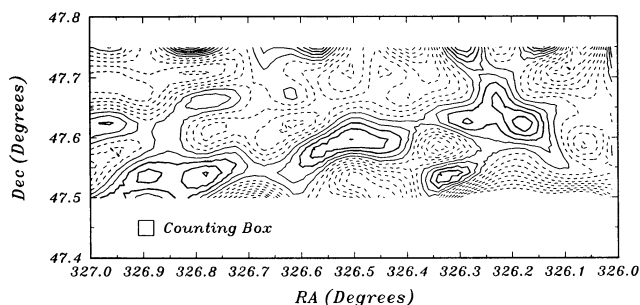


FIG. 3.—Map of the distribution of  $J$ -band star counts derived from the data plotted in Figure 2 using a 1.5 arc min size counting box and sampled at the Nyquist spatial frequency. The lowest contour is solid and corresponds to 2 counts. Subsequent solid contours increase in value in steps of 2 counts. The lowest dashed contour has a value of 12 counts and subsequent contours increase in steps of 2 counts.

square ranged from 0 to 30, with a mean of 12.5 stars for all 1026 boxes in the grid. Only three squares contained no stars.

Figure 3 shows the resulting contour map of the  $J$ -band star counts in the Northern Streamer. The contour map has been coded so that the regions of lowest surface density are more prominent. The solid contours trace out the regions of highest dust extinction in the cloud. We can convert the star counts to an extinction with knowledge of both the luminosity function and surface density of stars in the control field via

$$A_V = (A_V/A_J) \log (N_{\text{off}}/N_{\text{on}})/b_J,$$

where  $N_{\text{off}}$  is the surface density of stars in the control field,  $N_{\text{on}}$  is the corresponding surface density of stars (at any point) in the cloud,  $b_J$  is the slope of the cumulative  $J$  luminosity function of the stars in the control field, and the ratio  $A_V/A_J$  is the reddening law between  $V$  and  $J$  wavelengths. For our control field, we find that  $N_{\text{off}} = 20$  in a square box 1/5 on a side, and  $b_J = 0.36$  mag. The outermost solid contour represents a level of 10 counts and corresponds to a visual extinction of 3 mag. Within this contour level structure is clearly evident. Figure 4 shows a contour map of integrated CS emission presented at the same scale as the star count map. The CS emission traces dense ( $n_{\text{H}_2} \geq 10^4 \text{ cm}^{-3}$ ) molecular gas in the cloud. There is a good degree of similarity between the two maps, confirming our proposition that the infrared star counts are a good tracer of the dust distribution in the dense, inner portions of this dark cloud. Furthermore, the close similarity between the two maps suggests that a significant fraction of the stars observed are background field stars unrelated to the cloud.

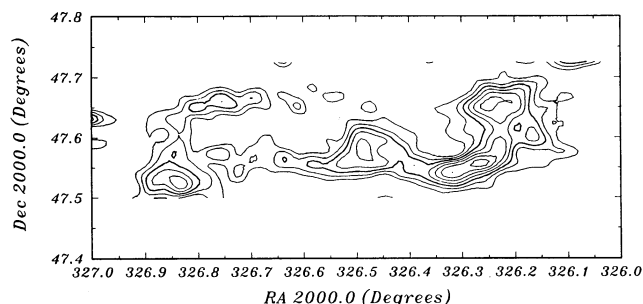


FIG. 4.—Contour map of CS ( $J = 2 \rightarrow 1$ ) emission presented at the same scale as Fig. 3 for comparison with the star count data. Coordinates are also epoch 2000.

Our observations represent a substantial improvement over previous star counting studies of molecular clouds, which were done exclusively at visual wavelengths (e.g., Dickman 1978; Cernicharo & Bachiller 1984). For example, consider the star counting study of the Taurus and Perseus molecular clouds by Cernicharo & Bachiller (1984), one of the most sensitive and extensive optical star counting studies ever done for a molecular cloud. In this study, a visual extinction of only 4.5 mag was typically sufficient to render a resau square of  $2.5 \times 2.5$  in size void of stars! For  $A_V \approx 3.5$  mag, only 1–2 optical stars were counted in such a  $2.5 \times 2.5$  square. However, we find that it requires visual extinctions in excess of roughly 17 mag to reduce our  $J$ -band counts to only 1–2 sources in a square of similar size. Thus, the dynamic range in visual magnitudes of extinction is at least a factor of nearly 5 greater than that of the Taurus-Perseus experiment. Consequently, our  $J$ -band star counts trace the distribution of dust to higher column densities with higher spatial resolution than has previously been possible in any molecular cloud.

### 3.2.2. Stellar Colors

The  $JHK$  infrared color-color diagram is a powerful tool for investigating the nature of stellar objects (Lada & Adams 1992). In Figures 5a and 5b, we show the  $JHK$  color-color diagrams for the control fields (Fig. 5a) and the Northern Streamer (Fig. 5b). These plots display only those stars in each region for which photometric uncertainties in each color were less than 0.10 mag. Also plotted in the figures are the locus of points corresponding to the unreddened main sequence and the locus of points corresponding to the positions of giant stars. Two parallel dashed lines form the reddening zone for main sequence stars. The bulk of the stars in the control field have colors of G-K stars. Many of these are presumably giant stars. Only a handful of stars fall in the infrared excess region to the right of the reddening zone. The two stars with the largest infrared excess were found to be doubles, with one component visible only in the  $K$  band. Of the roughly 900  $JHK$  stars observed with high-quality photometry toward the Northern Streamer, only a dozen or so show colors suggestive of significant infrared excess (none of these were obvious doubles). The vast majority of stars show normal stellar colors with various amounts of reddening. Comparison of the two diagrams strongly suggests that the vast majority of stars observed toward IC 5146 are field stars and unrelated to the cloud. Moreover, a significant number of these stars are clearly reddened background objects observed through the cloud.

## 4. ANALYSIS: THE COLOR EXCESS METHOD FOR EXTINCTION DETERMINATION

It has been recognized for some time that infrared colors could be used to directly measure the extinction and its distribution through a molecular cloud (e.g., Hyland 1980; Jones et al. 1981; Frerking et al. 1982). The line-of-sight extinction to an individual star can be directly determined from knowledge of its color excess and the extinction law. The color excess,  $E(H-K)$ , can be directly derived from observations, provided the intrinsic color of the star is known:

$$E(H-K) = (H-K)_{\text{observed}} - (H-K)_{\text{intrinsic}}. \quad (1)$$

The intrinsic  $(H-K)$  colors of normal main sequence and giant stars have a relatively small range: between 0.0 to 0.3 magnitudes for stars with spectral types between A0 and late M (e.g., Koornneef 1983). With the simple assumption that the



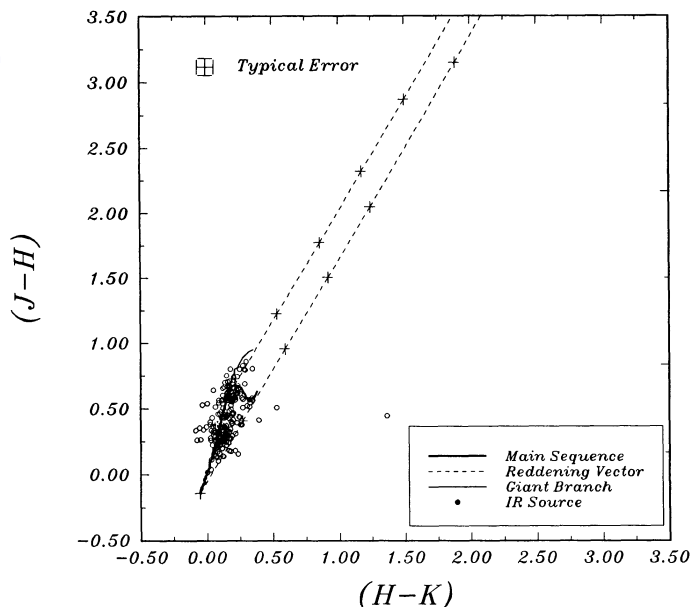


FIG. 5a

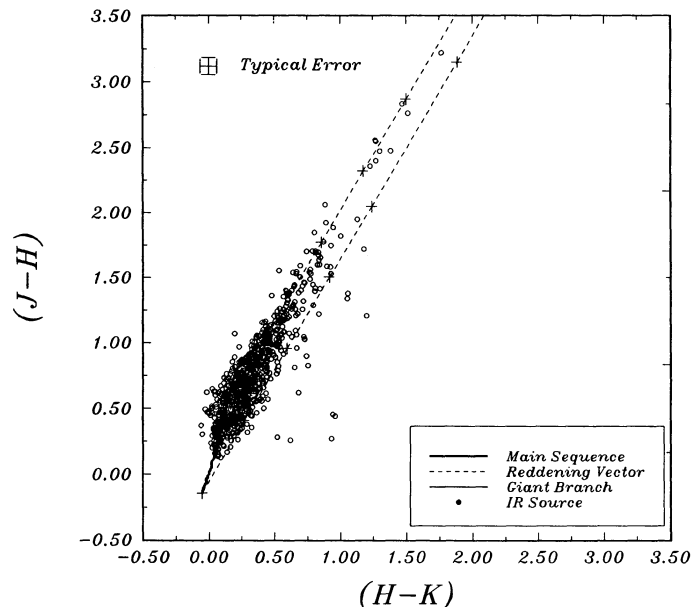


FIG. 5b

FIG. 5.—(a) *JHK* color-color diagram for the control field observations. (b) *JHK* color-color diagram for the stars in the Northern Streamer region. See text for discussion.

average  $(H-K)$  color of a typical field star is 0.15 mag, the maximum resulting uncertainty introduced to a determination of the *total* line-of-sight visual extinction ( $A_V$ ) would be only about 2.5 visual magnitudes. Clearly, more accurate color excess determinations are possible if the intrinsic colors of stars background to a target cloud are known. Observations of nearby control fields can be used very effectively to determine the intrinsic colors of background stars, provided that the control field stars do not themselves suffer significant random extinction.

Inspection of Figure 5a shows that the observed colors of the control field stars near IC 5146 are well constrained to normal, mostly main-sequence values. There is no evidence of any significant amounts of reddening in this color-color diagram. Therefore, with the assumption that all the stars observed toward the IC 5146 dark cloud are background field stars identical in nature to those in the control fields, we can use the mean  $(H-K)$  color of the control field stars to approximate the intrinsic  $(H-K)$  color of all stars background to the cloud:

$$(H-K)_{\text{intrinsic}} \equiv \langle (H-K) \rangle_{\text{control}} = 0.13 \pm 0.01 \text{ mag}. \quad (2)$$

This mean  $H-K$  color is equivalent to that of an early *K* star (Koornneef 1983; Bessel & Brett 1988). Using equations (1) and (2) we determined the color excess for 1295 stars with *H*- and *K*-band photometric uncertainties less than 0.15 mag observed in the direction of the Northern Streamer. Of these, all but about 30 stars were detected in all three infrared bands. Color excesses were determined for only those *JHK* stars which showed normal colors (i.e., stars with infrared excess were not included in the sample). Our database of color excesses and source positions represents a map of the distribution of color excess (and extinction) through the cloud which is obtained with very high spatial resolution (i.e.,  $1''$ – $2''$ ). However, this map is heavily undersampled, and the measurement points (stars) are distributed across it in a spatially nonuniform fashion. However, these data can be used to construct a

uniform and well-sampled map of the distribution of extinction through the cloud by effectively smoothing the angular resolution of the infrared observations to size scales comparable to the star count and millimeter-wave observations. To do this we binned the data in a manner analogous to star counting. That is, we scanned the map with a square spatial filter  $1.5 \times 1.5$  in size and sampled at the Nyquist (Spatial) frequency. Thus, we obtained the mean color excess of all the stars in the square, viz.,

$$\langle E(H-K) \rangle = \frac{\sum_{i=1}^N E(H-K)_i}{N}. \quad (3)$$

The result is a fully sampled, high-resolution map of the infrared color excess through the cloud. Since the infrared color excess is proportional to dust column density, this is equivalent to a map of dust column density through the cloud. Following convention, we find it convenient to represent the dust column density in terms of  $A_V$ , the extinction in the visual wavelength band, rather than color excess. The extinction at any wavelength is directly related to the color excess by a simple scale factor, which is given by the reddening law. Consequently, we converted the mean color excess at each point to an *equivalent visual* mean extinction using the normal reddening law (Rieke & Lebosky 1985):

$$\langle A_V \rangle = 15.9 \langle E(H-K) \rangle. \quad (4)$$

The resulting extinction map is displayed in Figure 6 and apart from the scale factor of 15.9 is identical to a map of color excess. The derived extinction ranges from about 1 magnitude to 40 magnitudes and corresponds to a variation in dust column density of about a factor of 40 from the low extinction outer regions of the cloud to the most opaque cores. The overall shape and structure in the map is very similar to both the *J*-band star count map and the CS map. By spatially integrating the extinction map, we can determine a very accurate

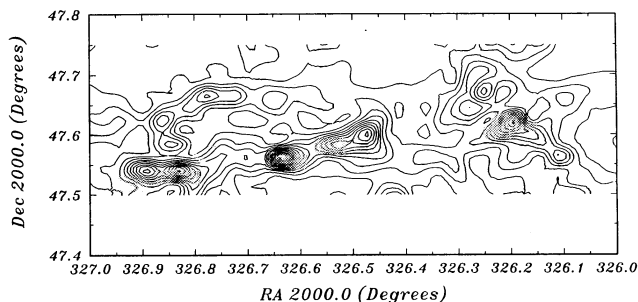


FIG. 6.—Map of the distribution of mean visual extinction,  $A_V$ , in the Northern Streamer derived from the infrared ( $H-K$ ) observations. The lowest contour corresponds to an extinction of 2 mag, and subsequent contours increase in steps of 2 mag. Similar to Fig. 3, the size of the measurement box (resolution) is  $1''.5$ , and the map represents data fully sampled at the Nyquist frequency.

(hydrogen) mass of the cloud, given a gas-to-dust ratio. Using the standard ratio (i.e.,  $N(\text{H} + \text{H}_2) = 2 \times 10^{21} \text{ cm}^{-2} \text{ mag}^{-1}$ ; see Lilley 1955; Bohlin et al. 1978), we derive the mass of the cloud to be  $M_{\text{IC 5146}} = 2800(D/1 \text{ kpc})^2 \pm 28(D/1 \text{ kpc})^2 M_{\odot}$ , for  $A_V \geq 4$  mag, the region of significant CS and  $\text{C}^{18}\text{O}$  emission (here  $D$  is the distance to the cloud). We note here that although the extinction map in Figure 6 accurately represents the variation of dust column density in the cloud, it corresponds to the true visual extinction through the cloud only to the extent that the reddening law in this cloud is a normal one (see following discussion). On the other hand, whether or not this cloud has a normal reddening law has no effect on our calculated hydrogen mass, since the gas-to-dust ratio we employed is calibrated in regions of low extinction, where the assumed normal reddening law applies.

## 5. INTERPRETATION AND DISCUSSION

### 5.1. Limitations and Uncertainties in the Method

When coupled with infrared array camera observations, the method of deriving extinctions from color excesses (equations [1]–[4]) becomes a very powerful and accurate technique for measuring and mapping the distribution of dust and hydrogen gas through a molecular cloud. However, the method is not without limitations or uncertainties. The uncertainties associated with this method fall into two categories. First, there are the uncertainties associated with the determination of color excess, and these are largely statistical in nature. Second, there are uncertainties introduced in the derivation of other physical quantities such as extinction, gas column density, and cloud mass from the color excess measurements. These latter uncertainties are largely systematic in nature. We consider and evaluate the two types of uncertainty separately as follows:

To determine the total (statistical) uncertainty  $\sigma_{\text{mean}}$  in our individual extinction measurements, we computed the dispersions ( $\sigma_{\text{disp}}$ ) in the extinction and the resulting error in the mean extinction ( $\sigma_{\text{mean}} = \sigma_{\text{disp}}/\sqrt{N}$ ) for each pixel in the map. These errors are actually errors in the color excess determinations but are expressed in terms of extinction after being scaled by the factor 15.9. In Figure 7 we plot  $\sigma_{\text{disp}}$  as a function of mean  $A_V$ . (The variation of  $\sigma_{\text{mean}}$  with  $A_V$  is virtually indistinguishable from that of  $\sigma_{\text{disp}}$  with  $A_V$ , apart from a  $\sqrt{N}$  reduction in scale.) We find the very interesting result that  $\sigma_{\text{disp}}$  (and  $\sigma_{\text{mean}}$ ) increase in a systematic fashion with increasing  $A_V$ .

Both trends are well fitted by linear relations:

$$\sigma_{\text{disp}} = (0.73 \pm 0.09) + (0.40 \pm 0.01)A_V, \quad (5)$$

$$\sigma_{\text{mean}} = (0.22 \pm 0.05) + (0.22 \pm 0.01)A_V. \quad (6)$$

Moreover, the dispersion in both relations (i.e., the dispersions in the quantities  $\sigma_{\text{disp}}$  and  $\sigma_{\text{mean}}$  themselves) also increases with  $A_V$ . In fact, the dispersion in  $\sigma_{\text{disp}}$  is a factor of 2.4 larger for  $A_V > 10$  mag than for  $A_V < 10$  mag.

There are several sources of uncertainty which are responsible for producing the form of the observed  $\sigma_{\text{disp}}-A_V$  and  $\sigma_{\text{mean}}-A_V$  relations. These include the following.

1. *Photometry.*—The fundamental source of statistical uncertainty is the photometric uncertainty in the infrared observations. These errors effectively set the lower limit to the amount of extinction which can be significantly measured. The measurement uncertainty for a given box or map pixel due to random photometric errors in the individual measurements is given by:  $\sigma_{\text{phot}} = (15.9/N) \sqrt{\sum_1^N [\sigma(H-K)_i^2 + \sigma(H-K)_{\text{intrinsic}}^2]} \approx 15.9\sigma_E/\sqrt{N}$  visual magnitudes, where  $\sigma(H-K)$  is the photometric error in the derived colors,  $\sigma_E = [\sigma(H-K)^2 + \sigma(H-K)_{\text{intrinsic}}^2]^{1/2}$  is the corresponding error in the color excess and  $N$  is the number of stars in the box. For values typical of the IC 5146 observations (i.e., 5% photometry, a 0.5% uncertainty in the intrinsic color excess, and  $N$  equal to the mean number [5] of stars in a box), we estimate a total photometric uncertainty of 0.5 mag in the mean  $A_V$  for a typical box. Consequently, our extinction measurements have a very high degree of confidence for  $A_V \geq 1.5$  mag. Since the data were filtered to include only observations of high photometric quality,  $\sigma_{\text{phot}}$  is not a strong function of  $A_V$ . These considerations indicate that for extinctions greater than about 5 mag, the total uncertainty is dominated by effects other than photometric errors.

2. *Background star colors.*—Because application of the color-excess method results in a determination of the line-of-sight extinction between the observer and the stars behind the

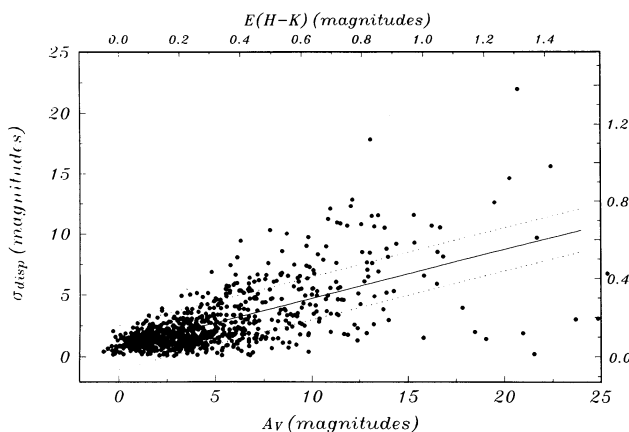


FIG. 7.—The variation of  $\sigma_{\text{disp}}$ , the dispersion in the extinction measurements, with  $A_V$  the derived mean extinction. Also plotted is the least-squares linear fit to the data over the entire range of extinction and the corresponding 1  $\sigma$  confidence bounds. The visual extinctions are derived from the observed color excesses assuming a normal reddening law, i.e.,  $A_V = 15.9 E(H-K)$ . The scale corresponding to the original color excess observations is also drawn. The dispersion in the measurements and  $\sigma_{\text{mean}}$ , the total uncertainty in the derived mean extinctions (and color excesses), are related as  $\sigma_{\text{mean}} = \sigma_{\text{disp}}/\sqrt{N}$ , where  $N$  is the number of stars used to derive the mean  $A_V$  for a given measurement box.



cold, variable reddening to the background stars produced by random, unrelated background and/or foreground dust clouds presents a major limitation to the application of this method. A reasonable application of this technique requires the dispersion in background field star ( $H-K$ ) colors to be smaller than the observed range in ( $H-K$ ) colors of the target stars. The dispersion in field star colors sets an additional lower limit to the extinction that can be reliably measured. Observations of control fields are necessary to establish the value of this limit. Clearly, for the IC 5146 control fields, where the dispersion in the ( $H-K$ ) color is only 0.08 magnitudes, our lower extinction limit is quite small, and this source of uncertainty is only important for derived extinctions less than about 1 mag. However, for many other molecular clouds, particularly in the first quadrant of the Galaxy, this will be a severe and limiting problem as can be ascertained from infrared observations of M17 (Lada et al. 1991) and NGC 6334 (Straw & Hyland 1989).

3. *Foreground/embedded stars.*—The color-excess method assumes that all the stars observed are background stars. Foreground stars or stars embedded in the cloud itself introduce additional uncertainties in the determinations. In particular, this method will not work for regions of molecular clouds containing embedded clusters (such as The Trapezium, NGC 2024, NGC 2264, and M17, etc), where the surface density of embedded stars exceeds that of background stars. However, for IC 5146, the effects of embedded stars have been minimized by the elimination of all stars with infrared excess from the sample; moreover, the general agreement of the star count maps with the molecular-line maps suggests that contamination from embedded stars is minimal. On the other hand, foreground star contamination may be a more significant source of error. Such stars will act to decrease the derived extinctions and will likely have a larger effect in regions of highest extinction. This would lead to an increase in  $\sigma$  with  $A_V$ , as is observed.

Our data can be used to make a reasonable estimate of the level of foreground star contamination. In regions of high extinction, the individual background stars should all be characterized by relatively high extinctions. Foreground stars should have colors indicative of zero extinction and should easily stand out among stars of high extinctions. We have examined the individual colors in all measurement boxes for which the derived mean  $A_V$  is greater than 9 mag. We searched these data for all zero-magnitude extinction stars. We conservatively defined a star to have zero extinction if its derived extinction was less than or equal to 4 times the total photometric uncertainty of the observations [i.e.,  $A_V(*) \leq 4\sigma_{\text{phot}}$ ]. In this manner we determined a firm upper limit to the mean number of foreground stars in a typical measurement box to be no greater than 0.32. This is small but not insignificant. The effect of the presence of such stars on  $\sigma_{\text{mean}}$  and  $\sigma_{\text{disp}}$  can be ascertained from modeling of the observations. We describe such modeling in the following section (§ 5.2) of this paper.

4. *Resolution and source structure.*—Because our method measures the mean extinction within a fixed area of the sky (box), uncertainties can be introduced if the extinction is not uniformly distributed across the measurement box. This can happen if the cloud is significantly structured or clumpy on scales smaller than the box size. Recent CO observations of IC 5146 obtained by Barnes Myers and Heyer (1994) at a resolution of  $55''$  show that there is structure on scales smaller than our 1.5 measurement boxes. Clearly, then cloud structure could have a significant effect on the  $\sigma$  vs.  $A_V$  relation for the Northern Streamer (eqs. [5] and [6]). However, the data can

be modeled to assess the significance of cloud structure on the observed errors and dispersions. In the next section of this paper, we describe such modeling, which indicates that the effects of small-scale cloud structure are primarily responsible for the form of the  $\sigma_{\text{disp}}-A_V$  relation for this source.

The sources of error discussed above are largely statistical in nature and pertain to the total uncertainty associated with the determination of the mean color excess  $\langle E(H-K) \rangle$ . The mean color excess is proportional to extinction, which is in turn proportional to dust column density and ultimately cloud mass. To express our results in terms of either extinction, column density, or mass, we need to know the corresponding constants of proportionality. Any uncertainties in these constants will introduce systematic uncertainties in the various derived quantities which depend on them. We now consider the major sources of systematic uncertainties in the various derived quantities.

1. *The reddening law.*—Extinction is directly related to color excess by the reddening or extinction law. We have chosen to scale the mean color excess to an *equivalent* visual extinction,  $A_V$ , using the standard extinction law. Our derived extinctions correspond exactly to the true *visual* extinction only if the extinction law for this cloud is normal. At visual and UV wavelengths the extinction law is known to vary along different lines of sight in the galaxy (Mathis 1990 and references therein), and, consequently, our derived *visual* extinctions will be systematically uncertain to the extent that the extinction law for this cloud departs from the standard law at visual wavelengths. However, in the near-infrared, the reddening law has been found to be universal with little, if any, variation along different lines of sight through the Galaxy (Mathis 1990 and references therein). Consequently,  $E(H-K)$  can be scaled confidently to an infrared extinction (e.g.,  $A_K$ ) using a standard (normal) extinction law (e.g.,  $A_K = 1.78 E(H-K) = 0.112 A_V$ ; see Rieke & Lebofsky 1985), and the use of a standard extinction law does not introduce significant uncertainties in any of the masses or column densities derived from the mean color excess method.

2. *Gas-to-dust ratio.*—The total hydrogen column density for a map pixel is determined by scaling the extinction there by the gas-to-dust ratio,  $R_{g-d}$ . Similarly, determining the total mass of the cloud also depends directly on this ratio. There is considerable evidence to suggest that  $R_{g-d}$  is constant or universal in the Galaxy at relatively low extinctions (i.e.,  $A_V \leq 2$  mag; see Lilley 1955; Bohlin et al. 1978; Savage & Mathis 1979). It is not clear if the ratio will change at high extinctions such as those characterizing the most opaque regions of IC 5146. Theoretical justification for a constant ratio at high extinctions has been discussed by Dickman (1978) and will not be considered here. In any event, our mass and hydrogen column density determinations are systematically uncertain to the extent that the gas-to-dust ratio in this source departs from the universal value.

3. *Distance.*—By far the most uncertain quantity we derive from our data is the mass of the cloud. This is because the distance to the cloud is the largest source of systematic uncertainty in the mass determinations. The uncertainty in the mass of the cloud is given by

$$\begin{aligned} \sigma(\text{mass}) &= R_{g-d} l^2 D^2 \sigma[\Sigma(A_V)] \\ &= 0.25 R_{g-d} D^2 l^2 \left\{ \sum_{i=1}^n [\sigma_i(\text{tot})]^2 \right\}^{0.5}, \end{aligned}$$

where  $D$  is the distance to the source,  $l^2$  is the area of a single

measurement box (in square radians), and the factor 0.25 is a correction for oversampling. For the regions with  $A_V > 4.0$  mag, we find the fractional statistical uncertainty,  $\sigma[\Sigma(A_V)]/\Sigma(A_V)$ , to be only 1%. The distance to the Northern Streamer is usually assumed to be the same as that (900 pc) derived optically for the cluster IC 5146 (e.g., Elias 1978; Dobashi et al. 1992). Although the cluster is at a relatively large projected distance from the Northern Streamer, this assumption seems justified by the presence of a bridge of  $^{12}\text{CO}$  and  $^{13}\text{CO}$  emission which appears to connect the cluster and the streamers (Fig. 1; see also Dobashi et al. 1992). However, the relative lack of foreground stars toward the dark clouds which make up the Northern Streamer suggests a distance closer than 900 pc. Indeed, if the predictions of the Bahcall & Soneira (1980) model of the Galaxy are scaled to our control field observations, we find that we expect to observe an average of 2.1 foreground stars in a typical 1.5 measurement box in this direction of the Galaxy for a 1 kpc distance to the cloud. To reduce this to a number close to that actually estimated from our observations (see above) requires the cloud to be at a distance of about 400 pc. Consequently, we consider the distance to the Northern Streamer to be highly uncertain and probably smaller than the 900 pc usually quoted in the literature.

### 5.2. Modeling and Cloud Structure

It is possible to predict the form of the  $\sigma_{\text{disp}}-A_V$  relation by modeling the structure of the cloud and the foreground star distribution. In the case where the foreground star contribution is small or known, the  $\sigma_{\text{disp}}-A_V$  relation can be used to derive direct and quantitative information about the nature of the spatial distribution of dust on scales smaller than our effective binning box resolution.

We constructed Monte Carlo models to mimic the infrared observations and predict  $\sigma_{\text{disp}}-A_V$  curves for various cloud configurations. We first assumed that the spatial distribution of dust had the same functional form in all 1000 measurement boxes. However, the model boxes differed from one another in the total amount or mean extinction contained within them. This mean extinction was varied from 0–25 mag. Between these two limits of mean extinction, the boxes were divided equally into bins 0.2 mag wide. To obtain a measurement of mean extinction which corresponded to that derived from observations, model stars were randomly generated and placed within each counting box. The extinction to each star was calculated from the input dust distribution assuming that the stars were background objects. Noise, simulating photometric measurement errors was also added to each star's extinction value. The mean extinction and its dispersion were calculated for all the stars in each box. To determine the number of stars to be placed in each box we assumed a Poisson distribution with a mean of 5, similar to the observed value. For each extinction step, typically seven boxes of stars were created and measured. The results were then plotted in the form of a  $\sigma_{\text{disp}}-A_V$  relation similar to the observations.

Figure 8 shows the  $\sigma_{\text{disp}}-A_V$  relation for the case of a uniform distribution of extinction in each box and no foreground stars. The predicted dispersions are constant and independent of  $A_V$  with an internal scatter also independent of  $A_V$  and consistent with that expected solely from the photometric errors introduced in the model. This is clearly different from the observations of IC 5146. It is possible that the presence of foreground stars in the measurement boxes could account for some of the

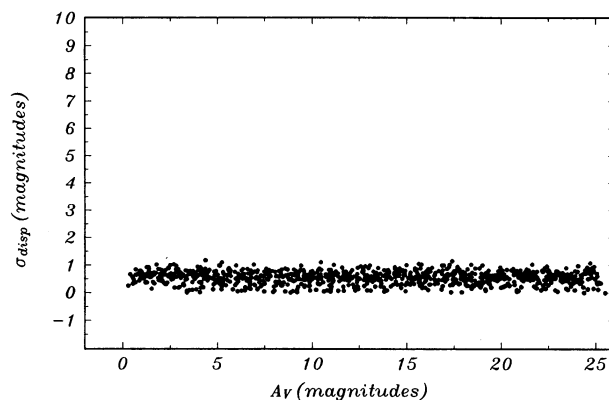


FIG. 8.—The variation of  $\sigma_{\text{disp}}$ , the dispersion in the individual mean extinction measurements, with mean  $A_V$  predicted by a model characterized by uniform cloud structure within each measurement box. Comparison with Fig. 7 suggests that the spatial distribution of extinction is not uniform on angular scales smaller than that of the observations (i.e., 1.5).

effects which characterize the observed  $\sigma_{\text{disp}}-A_V$  relation. To investigate this possibility, foreground stars were added to the model by assuming that they had zero mean extinction plus some measurement noise and that their probability of being found in a measurement box was given by a Poisson distribution function with a mean of 0.32, corresponding to observations. The resulting  $\sigma_{\text{disp}}-A_V$  relation is shown in Figure 9. The inclusion of foreground stars alters the relation between dispersion and extinction, but again the relation has little resemblance to the actual observations. These results rule out models for cloud structure which assume a uniform spatial distribution of dust on scales smaller than a box size (i.e.,  $\leq 1.5$ ). These results also indicate that cloud structure is likely more important for determining the form of the observed  $\sigma_{\text{disp}}-A_V$  relation than is foreground star contamination.

Since uniform extinction models can not account for the observations, we investigated other classes of models which describe different spatial distributions of dust. Figure 10 shows the resulting  $\sigma_{\text{disp}}-A_V$  relation for models which assume that the dust is distributed in discrete, high extinction clumps

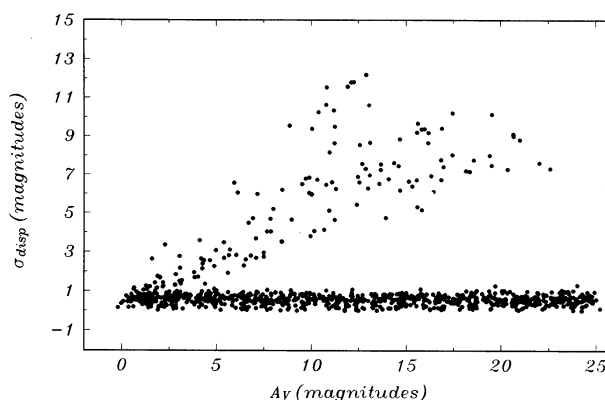


FIG. 9.—The variation of  $\sigma_{\text{disp}}$ , the dispersion in the individual mean extinction measurements, with mean  $A_V$  predicted by models of uniform cloud structure with a small contribution from foreground stars within each measurement box. The surface density of foreground stars was set to equal that inferred from observations. Comparison with Fig. 7 suggests that the addition of foreground stars cannot explain the observed data and that the observed form of the  $\sigma_{\text{disp}}-A_V$  relation must be largely a result of small-scale variations in cloud structure and not due to the presence of foreground stars.

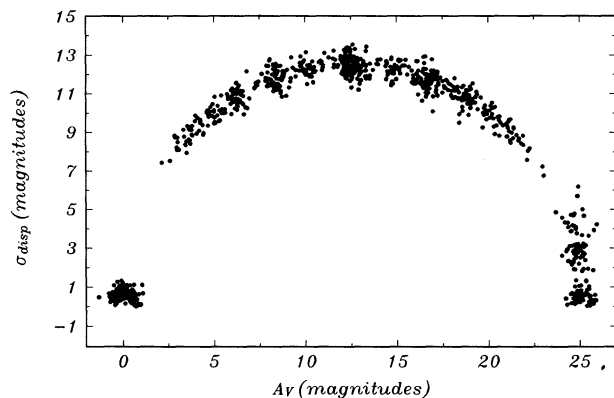


FIG. 10.—The variation of  $\sigma_{\text{disp}}$ , the dispersion in the individual mean extinction measurements, with mean  $A_V$  predicted by models of in which the measurement boxes are filled with discrete high extinction clumps with zero extinction interclump material between them. The mean extinction derived for a measurement box in such a model depends only on the filling factor of the clumps. Comparison with Fig. 7 clearly rules out this form of clumpiness in the cloud.

(baseballs) with zero extinction (air) between them. In these models, the mean extinction in a box is directly related to the filling factor of the clumps, which is varied from zero to unity in order to span the range of observed extinctions. As in the models shown in Figure 9, the contribution of foreground stars was also included. The data in Figure 7 clearly rule out this class of models.

To examine other possible variations in the surface density distribution of extinction in the cloud, we investigated a class of models in which the extinction distribution in each box was described by a two-dimensional power-law function of the form  $A_V(x, y) \propto x^\alpha y^\alpha$  with initially no foreground stars. Only three parameters were needed to characterize each model,  $\sigma_{\text{phot}}$ ,  $\alpha$ , and  $A_0$ , the extinction in a box. The value of  $A_0$  was fixed, and the other two parameters were varied until the slope and the intercept of the linear fit to the  $\sigma_{\text{disp}}-A_V$  relation matched those derived from observation (0.73 mag and 0.40, respectively). The observed data were found to be well

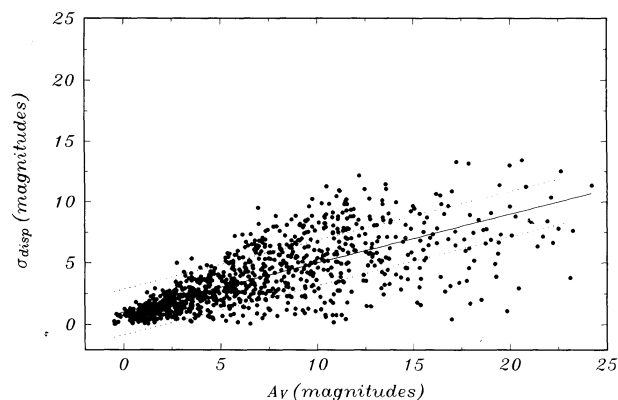


FIG. 11.—The variation of  $\sigma_{\text{disp}}$ , the dispersion in the individual mean extinction measurements, with mean  $A_V$  predicted by models in which the surface density of extinction within each measurement box spatially varies in a power-law fashion. This particular model of cloud structure closely matches the data. This model also includes a contribution from foreground stars. See text for discussion.

modeled by a surprisingly narrow range of these parameters:  $\alpha = 0.85 \pm 0.05$ , and  $\sigma_{\text{phot}} = 0.5 \pm 0.2$ . The model data for  $\alpha = 0.85$ , and  $\sigma_{\text{phot}} = 0.5$  are shown in Fig. 11 where we have also included the contribution of foreground stars. The general agreement with the data is remarkable, although we do find that the fits are not as nearly well constrained if the contribution due to foreground star contamination is allowed to vary in any significant way. The physical significance of this particular set of cloud models and their agreement with observations is not clear from the present analysis. Nonetheless, it seems clear that simple models of uniform dust distribution and clumpiness are ruled out by our observations. Moreover, foreground star contamination alone cannot account for the observed relations present in the data.

Finally, we note that cloud structure variations are also a significant source of uncertainty for interpreting star count data or molecular line observations made with single aperture telescopes, whose resolution is large compared to interesting physical structure. However, unlike these techniques, which are inherently incapable of sensing such difficulties, the color excess method for deriving extinctions presented here provides a *quantitative* assessment of the magnitude of such uncertainties and in the process an additional probe of the cloud structure itself. This is a major advantage of this method of measurement. Our results also suggest that foreground star contamination can be a serious problem in some instances. Such contamination can also present major limitations for star count measurements as can be ascertained from the star count maps of the Orion Cloud (Rosanno 1980). However, the foreground contribution to star counts cannot be determined from star count data alone.

### 5.3. Comparison of the Molecular-Line and Extinction Data

Figure 12 shows our map of integrated  $\text{C}^{18}\text{O}$  emission (between 2 and 6  $\text{km s}^{-1}$ ) of the Northern Streamer drawn on the same scale as the extinction map (Fig. 6). The general appearance of the two maps is remarkably similar. This is not entirely unexpected, since both maps trace column density. Comparison of the two maps provides direct information on the dust-to-(CO) gas ratio and its constancy through the cloud. In order to facilitate a more detailed comparison of the extinction and molecular-line data, we constructed an additional extinction map of the cloud with the same angular resolution (1'7) and grid spacing (1') as the molecular line maps. In Figures 13, 14, and 15 we show the relation between visual extinction and the integrated intensities (between 2 and

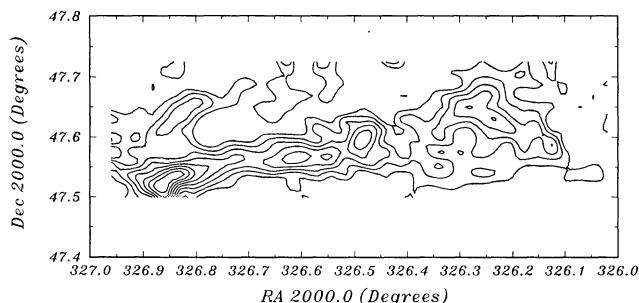


FIG. 12.—Map of the integrated  $\text{C}^{18}\text{O}$  ( $J = 1 \rightarrow 0$ ) emission in the Northern Streamer presented on the same scale as Figs. 2, 3, 4, and 6 for comparison. The lowest contour corresponds to 0.1  $\text{K km s}^{-1}$ . Subsequent contours increase in equal steps of 0.3  $\text{K km s}^{-1}$ .



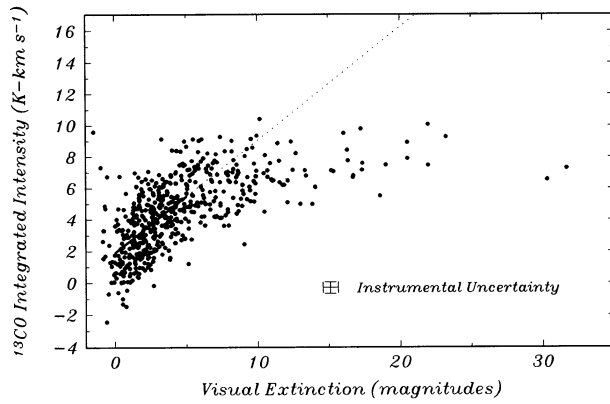


FIG. 13.—Comparison of the  $^{13}\text{CO}$  integrated intensity with visual extinction in the Northern Streamer cloud. Also plotted is the line corresponding to the least-squares linear fit to the data between 0 and 5 mag.

$6 \text{ km s}^{-1}$ ) of  $^{13}\text{CO}$ ,  $\text{C}^{18}\text{O}$  and CS at the more than 500 positions where common data were obtained.

In order to quantify the various correlations, we performed linear least-square fits over varying ranges of  $A_V$  for all three molecular lines. We found that the  $^{13}\text{CO}$  emission could be fitted by a linear relation with a constant slope from zero up to 5–6 mag of extinction. For maximum extinction values larger than about 8 mag, the values of the derived slope significantly decreased, and the quality of the fit decline considerably. We conclude that the  $^{13}\text{CO}$  integrated intensity is roughly linearly correlated with  $A_V$  between 0 and about 5 mag. When extinctions reach between 8 and 10 mag, the  $^{13}\text{CO}$  emission appears saturated. Both  $\text{C}^{18}\text{O}$  and CS emission could be reasonably fitted by linear relations with  $A_V$  over the entire range of observed extinctions. In both cases, the slopes of the fitted relations are constant for fits spanning ranges of  $A_V$  from 0 up to 15 mag. However, the slopes of the fits performed over increasingly larger ranges of extinction are found to decrease. This decrease in slope could be caused by opacity effects which begin to set in for these molecules at about 15 mag of visual extinction or a decrease in their relative abundances at large extinctions. In addition, the relatively large uncertainties in  $A_V$  at large extinctions could also contribute to a change in slope

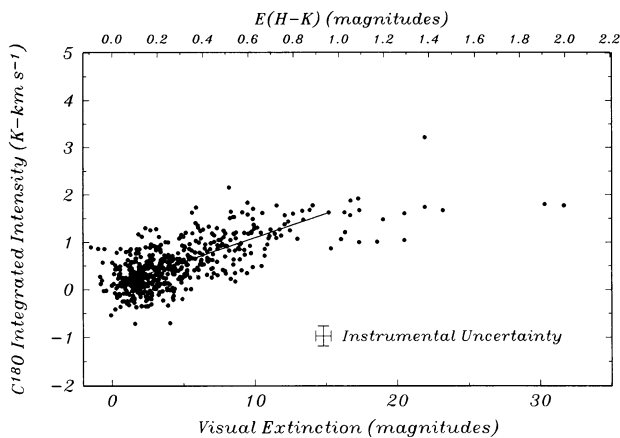


FIG. 14.—Comparison of the  $\text{C}^{18}\text{O}$  integrated intensity with visual extinction (and color excess) in the Northern Streamer cloud. Also plotted is the line corresponding to the least-squares line fit to the data between 0 and 15 mag.

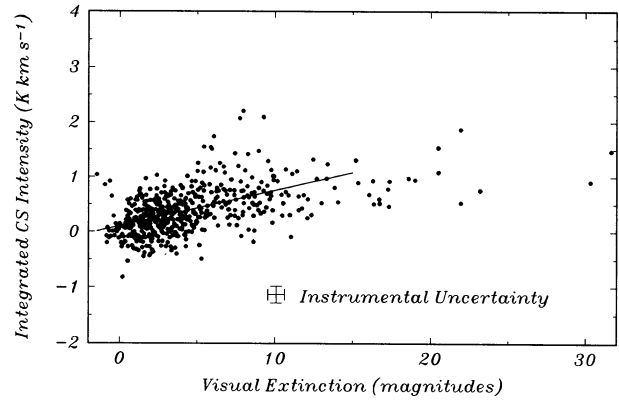


FIG. 15.—Comparison of the integrated CS emission with visual extinction in the Northern Streamer cloud. Also plotted is the line corresponding to the least-squares linear fit to the data between 0 and 15 mag.

at large  $A_V$ . The derived linear fits for the three molecules are

$$I(^{13}\text{CO}) = 1.88 \pm 0.17 + (0.72 \pm 0.06)A_V \text{ K km s}^{-1} \quad (A_V \leq 5 \text{ mag}),$$

$$I(\text{C}^{18}\text{O}) = 0.07 \pm 0.03 + (0.10 \pm 0.01)A_V \text{ K km s}^{-1} \quad (A_V \leq 15 \text{ mag}),$$

$$I(\text{CS}) = 0.10 \pm 0.02 + (0.06 \pm 0.01)A_V \text{ K km s}^{-1} \quad (A_V \leq 15 \text{ mag}).$$

We observe large scatter in all three relations. Such large scatter also characterizes similar relations derived from star count studies (e.g., Dickman 1978; Bachiller & Cernicharo 1986; Langer et al. 1989, etc.). The scatter in these relations has two possible origins: it can be intrinsic and/or the result of experimental (instrumental) uncertainties. Instrumental uncertainties give rise to scatter in the determinations of both integrated intensity and extinction. The instrumental uncertainty,  $\sigma_{ii}$ , in the integrated intensity for each molecular-line spectrum was determined by integrating over a  $4 \text{ km s}^{-1}$  wide region of the spectrum well outside the velocity limits of observed molecular emission. The instrumental uncertainty in the extinction,  $\sigma_{\text{phot}}$ , was determined in the manner described earlier in this paper. As discussed earlier, there are additional uncertainties in the extinction measurements due in most part to variations in cloud structure on small angular scales. These uncertainties become important for  $A_V > 5 \text{ mag}$ .

The size of the typical instrumental uncertainties in integrated intensities and extinction are plotted in Figures 13–15. In all three cases, the scatter appears larger than allowed by the instrumental errors. Moreover, the scatter in the  $^{13}\text{CO}$  versus  $A_V$  plot (Fig. 13) appears to be considerably larger than that exhibited in the corresponding  $\text{C}^{18}\text{O}$  and CS plots (Figs. 14 and 15). Indeed, we find that the dispersion of the residuals,  $\sigma_{\text{residuals}}$ , of each of the above linear least-square fits is greater than the corresponding  $\langle \sigma_{ii} \rangle$ , the mean uncertainty in integrated intensity, by factors of 4.8, 1.6, and 2.2 for  $^{13}\text{CO}$ ,  $\text{C}^{18}\text{O}$ , and CS observations, respectively. This suggests that the origin of the large scatter in the  $^{13}\text{CO}$  versus  $A_V$  relation is intrinsic and not the result of any additional uncertainties in extinction measurements introduced by variations in cloud structure. The origin of such intrinsic scatter is astrophysical in nature and likely due to intrinsic variations in the excitation or abundance

of the molecule through the cloud. Consequently, it would appear that there is an inherent uncertainty (of roughly a factor of 5) in using  $^{13}\text{CO}$  observations to derive a hydrogen column densities along a given line of sight within a molecular cloud.

Direct comparison of  $\text{C}^{18}\text{O}$  and CS emission throughout the cloud suggests that the larger-than-expected scatter in Figures 14 and 15 is also due to intrinsic variations in the excitation or abundances of the two molecules. The emission from the two species is found to be linearly correlated with a scatter which is independent of the strength of the emission and whose dispersion (i.e.,  $\sigma_{\text{residuals}}$ ) is a factor of 2 greater than the mean uncertainties in the integrated intensities of each line. Evidently,  $\text{C}^{18}\text{O}$  observations can be more reliably used to determine hydrogen column densities and molecular cloud mass than  $^{13}\text{CO}$  observations, however, inherent uncertainties on the order of a factor of 2 are still present even for this tracer.

Finally, we note that in all three cases the fits have intercepts that are positive. This results in the uncomfortable prediction of molecular emission at an extinction of zero magnitudes. This could be produced by a zero-point error in either the extinction or molecular-line measurements or by some measurement bias at low extinctions and/or integrated intensities. We have not identified any such effects in our data, and at the present time we have no explanation for this property of the fits. We did investigate the possibility of a mismatch between our square measurement box and the Gaussian radio telescope beam, which is sensitive to emission, located outside its half-power beamwidth and beyond the area of the measurement box. To investigate this possibility we doubled the area of the measurement box and redetermined the extinctions at each point in the  $^{13}\text{CO}$  grid. This larger box had diameter of 2.4. Fitting the integrated intensity versus extinction data over similar ranges in extinction, we found that the intercepts of the fits typically decreased in value but still remained positive when the larger box size was used.

#### 5.4. Molecular Abundances

The ultimate goal of comparison of molecular-line emission with extinction measurements is to determine directly the abundance of each molecule relative to hydrogen. Until now, such determinations have been made at relatively low extinctions (0–4 mag; e.g., Dickman 1978; Minn & Greenberg 1979; Sandell et al. 1981; Bachiller & Cernicharo 1984; Mattila 1986; Duvert, Cernicharo, & Baudry 1968; Langer et al. 1989, etc.) Our extinction map of IC 5146 offers the possibility of making such determinations not only in more opaque regions of a molecular cloud, but also, for the first time, for molecules, such as CS, which require high densities for excitation.

In principle, we can convert our integrated intensities to molecular column densities at each point in the map, compare these to the  $(H-K)$  derived extinctions and thereby directly measure the abundance of each molecule at over 500 locations in the cloud. However, with the current single-transition molecular-line data set we are limited to determining LTE column densities for each of the observed molecules. We expect that non-LTE effects may be operating in the cloud, and LTE column density estimates are likely to be somewhat inaccurate. Nonetheless, the LTE column densities for each molecule were calculated at each point in the cloud, assuming that the excitation temperature of  $^{13}\text{CO}$  and  $\text{C}^{18}\text{O}$  is the same as that of  $^{12}\text{CO}$ , which has been measured by Dobashi et al. (1993) to be about 10 K, and, in addition, found to be constant throughout the cloud to a good approximation. For the CS emission, we

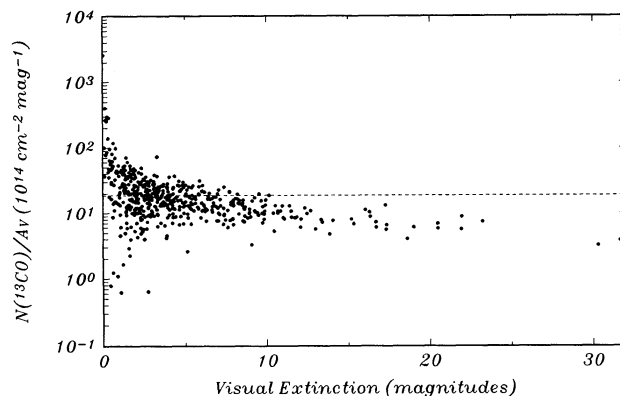


FIG. 16.—The variation of the  $N(^{13}\text{CO})$  LTE column density to  $A_V$  ratio with extinction. The dashed line represents the mean value of the ratio determined between 0–5 mag, where the  $^{13}\text{CO}$  emission is optically thin.

assumed that the levels were subthermally excited and that the excitation temperature was only 5 K. We also calculated the LTE column densities of CS assuming an excitation temperature of 10 K, and the results were not significantly different from the LTE calculations based on a 5 K temperature.

We obtained the ratio of LTE molecular column density to  $A_V$  at each point in the cloud for each molecule. The results are displayed in Figures 16, 17, and 18, where we plot this ratio versus extinction for  $^{13}\text{CO}$ ,  $\text{C}^{18}\text{O}$ , and CS, respectively. For each molecule we obtained the mean abundance ratio over the range for which the integrated intensities were found to be linearly correlated with extinction:

$$\langle N(^{13}\text{CO})_{\text{LTE}}/A_V \rangle = 2.18 \pm 0.24 \times 10^{15} \text{ cm}^{-2} \text{ mag}^{-1} \quad (A_V \leq 5 \text{ mag}),$$

$$\langle N(\text{C}^{18}\text{O})_{\text{LTE}}/A_V \rangle = 2.29 \pm 0.72 \times 10^{14} \text{ cm}^{-2} \text{ mag}^{-1} \quad (A_V \leq 15 \text{ mag}),$$

$$\langle N(\text{CS})_{\text{LTE}}/A_V \rangle = 4.5 \pm 0.9 \times 10^{11} \text{ cm}^{-2} \text{ mag}^{-1} \quad (A_V \leq 15 \text{ mag}).$$

This mean ratio is shown in each figure as a dashed horizontal line. We also determined, in a similar manner, the

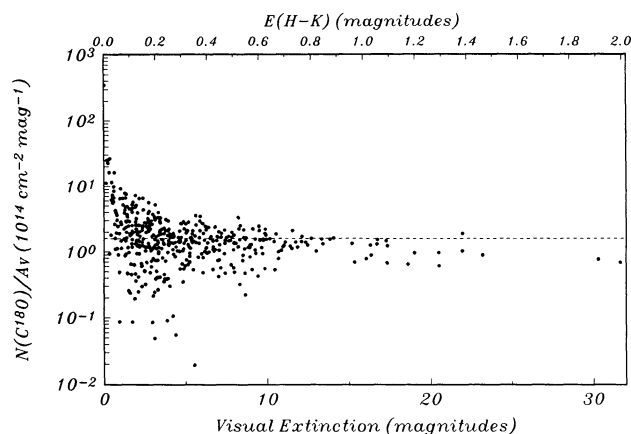


FIG. 17.—The variation of the  $N(\text{C}^{18}\text{O})$  LTE column density to  $A_V$  ratio with extinction and color excess. The dashed line represents the mean value of the ratio determined between 0–15 mag, where the  $\text{C}^{18}\text{O}$  emission is optically thin.

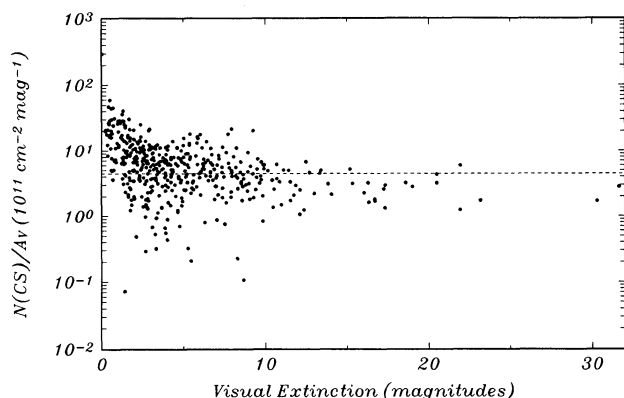


FIG. 18.—The variation of the  $N(\text{CS})$  LTE column density to  $A_V$  ratio with extinction. The dashed line represents the mean value of the ratio determined between 0–15 mag, where the CS emission is optically thin.

$N(^{13}\text{CO})/A_V$  ratio using extinctions derived with a 2/4 size measuring box and found the ratio to be within 10% of the value quoted above for the 1/7 boxes. We note that for  $^{13}\text{CO}$ , the calculated abundance ratio falls about a factor of 6 below the mean value at the highest extinctions, illustrating once more the effects of high optical depths on the  $^{13}\text{CO}$  emission. Clearly,  $^{13}\text{CO}$  is not a good tracer of gas column density at extinctions much greater than about 10 mag. On the other hand, the derived LTE abundances of  $\text{C}^{18}\text{O}$  and CS at the highest extinctions are within only a factor of 2 of the estimated mean value, and this is less than the overall scatter in the calculated ratios.

It is instructive to investigate the relative abundance of  $^{13}\text{CO}$  and  $\text{C}^{18}\text{O}$  as a function of cloud depth. In Fig. 19 we plot the mean ratio of the  $^{13}\text{CO}$  and  $\text{C}^{18}\text{O}$  column densities as a function of  $A_V$ . This ratio has been computed by binning the individually calculated ratios into intervals of  $A_V$  3 mag in width and taking the mean value of the ratio in each extinction bin. The upper curve shows the ratio of the column densities; the lower plot shows the calculated dispersion in this ratio. In the outer parts of the cloud (i.e.,  $A_V \leq 10$  mag) the  $^{13}\text{CO}$  to  $\text{C}^{18}\text{O}$  column density ratio is large, considerably greater than the terrestrial ratio of 5.5. Such large ratios were also found at low extinctions in the studies of Bachiller & Cernicharo (1986)

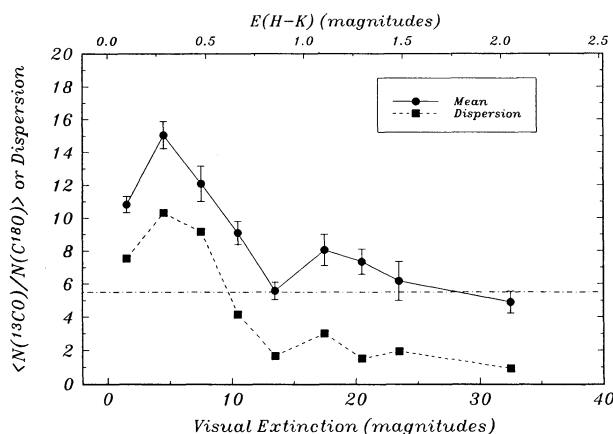


FIG. 19.—The variation of the mean  $N(^{13}\text{CO})/N(\text{C}^{18}\text{O})$  column density ratio and its dispersion with extinction (and color excess) in the cloud. The horizontal line at a value 5.5 represents the terrestrial value of this ratio. See text for discussion.

and Frerking et al. (1982) and are indicative of enhanced  $^{13}\text{CO}$  abundances, presumably due to some combination of chemical fractionation of  $^{13}\text{CO}$  and selective photodissociation of  $\text{C}^{18}\text{O}$  (e.g., van Dishoeck & Black 1988). For  $A_V$  greater than 10 mag, the column density ratio is essentially terrestrial. However, it is somewhat difficult to interpret the significance of this, given that the  $^{13}\text{CO}$  emission is optically thick in these regions of the cloud. (We note that over the same  $A_V$  intervals, the mean integrated intensity ratio of the two species varies in a very similar manner from values of roughly 14 to 4). However, what is striking about Fig. 14 is that the dispersion in the ratio of the column densities is also a strong function of extinction. In the outer parts of the cloud, the dispersion is very large, while beyond 10 mag depth it is small. This strongly suggests that the abundances of one or both of the species of CO are unstable in the outer parts (i.e.,  $A_V < 10$  mag) of the cloud, probably due to active chemical processing by UV radiation. For visual extinctions greater than 10 mag, the  $\text{C}^{18}\text{O}$  and  $^{13}\text{CO}$  abundances appear quite stable.

### 5.5. Comparison With Previous Studies

It would be useful to compare the abundances derived in this study to abundances derived using traditional optical star count methods. Unfortunately, such abundance studies do not exist for this cloud. However,  $^{13}\text{CO}$  abundances derived from star count studies have been reported for a number of other molecular clouds. These LTE abundances compare well to those derived here for IC 5146 (e.g., Irvine, Goldsmith, & Hjalmarson 1987; Bachiller & Cernicharo 1986). In particular, the mean  $^{13}\text{CO}$  abundance derived by Dickman (1978) for a heterogeneous sample of molecular clouds using star counts is essentially the same as our  $^{13}\text{CO}$  abundance determination for the Northern Streamer of IC 5146. Our abundance also appears to be similar to those derived from star count studies of the Perseus dark clouds (Bachiller & Cernicharo 1986), the Ophiuchi dark clouds (Dickman & Herbst 1990), the L1495 dark cloud (Duvert et al. 1986), and B5 (Langer et al. 1989). Similarly, our  $\text{C}^{18}\text{O}$  abundances compare well to those derived from star counts for L 1495 (Duvert et al. 1986) and B5 (Langer et al. 1989). However, it is not clear how much weight should be attached to the apparent similarity in derived abundances between our study and previous work. Except for Dickman (1978), the abundances quoted in star count studies are derived from the slopes of linear fits to column density versus extinction plots, whereas in this study and in Dickman (1978), the abundance is derived from direct averaging of the individual determinations. In principle, both determinations should give the same result. However, we found that although our linear fits to the various column density versus extinction relations indicated that the quantities were correlated to a very high probability, the fits were also characterized by relatively low correlation coefficients (0.5–0.7). This suggested that using the slopes of the relations to derive abundances could introduce relatively large (a factor of 2) uncertainties. Consequently, we adopted the abundances derived from averaging the individual determinations through the cloud. These abundance determinations were typically a factor of 1.5–2 times greater than those we derived from the slopes of linear fits to the column density versus  $A_V$  relations for each molecule.

It is perhaps most interesting to compare our results to those of Frerking et al. (1982), who derived  $^{13}\text{CO}$  and  $\text{C}^{18}\text{O}$  abundances in the Taurus and Ophiuchi clouds also using infrared



color-excesses of background stars. Their methodology was very similar to ours, except that they measured the colors of only a single star at the position of each CO observation. Moreover, they were only able to determine extinctions toward roughly a dozen stars of known spectral type in each of the clouds and were not able to map the distributions of extinctions. However, they were able to determine the abundance of  $^{13}\text{CO}$  in Taurus along lines of sight showing  $A_V$ 's of about 20 mag. Although they measured the abundances toward only about a dozen stars, their plot of  $N(^{13}\text{CO})$  versus  $A_V$  for the Taurus clouds reveals all the same important qualitative features as we find for IC 5146 from Figure 8 of this paper (i.e., a more or less linear correlation of  $^{13}\text{CO}$  column density, with  $A_V$  up to about 5 mag with clear evidence for effects of saturation at higher extinctions). However, the overall  $^{13}\text{CO}$  abundance they derive appears to be about a factor of 2 lower than that we have derived for IC 5146. On the other hand, for Ophiuchus, where their measurements extended out to an  $A_V$  of only about 10 mag, they derive a similar  $^{13}\text{CO}$  abundance as derived here but find that the  $^{13}\text{CO}$  column density appears to be linearly correlated with extinction out to 10 mag, a result similar to that reported by Dickman & Herbst (1990). Our data could also be fitted by a linear function out to 8–10 mag, but the resulting slope is significantly flatter than that derived for the 0–5 mag range, and this suggests that caution needs to be applied when extending such relations beyond 5–6 magnitudes of visual extinction. The abundances Frerking et al. (1982) derived for  $\text{C}^{18}\text{O}$  in Taurus and Ophiuchus are quite similar to those derived here for IC 5146.

Our CS abundance determination is the first direct CS abundance determination to be made for a dense molecular cloud. Prior determinations of CS abundances in dark clouds have been accomplished by comparing the derived CS column density with an estimate of the molecular hydrogen density, which is indirectly derived either from excitation calculations or by a direct comparison with the observed column density of another molecule, such as  $\text{C}^{18}\text{O}$ , whose abundance relative to  $\text{H}_2$  is assumed to be known (e.g., Swade 1989). To date, almost all such determinations have been made in warm ( $T_K \approx 20$ –50 K), massive, and dense cores such as Orion and M17, which have significant star-formation activity within them. The derived CS abundances in these regions is about an order of magnitude larger than derived here for the Northern Streamer (e.g., Irvine et al. 1987 and references therein), although there are large variations in these measurements. On the other hand, our derived CS abundance is comparable to that ( $\sim 5 \times 10^{-10}$ ) recently derived for the dark cloud L134N by Swade & Schloerb (1992) from observations and analysis of the CS  $J = 2 \rightarrow 1$  and  $J = 3 \rightarrow 2$  transitions.

## 6. SUMMARY AND CONCLUSIONS

We have developed a method which uses observations of the infrared color excesses of background stars to directly measure and map the distribution of dust extinction through a molecular cloud. Because infrared excess is directly proportional to extinction, this method provides a more direct and accurate measure of extinction than does star counts. Moreover, because the infrared color excess is also proportional to dust column density, the derived extinction map reflects the actual distribution of dust through a cloud. We have applied this technique to determine the distribution of extinction in a dark cloud near the cluster IC 5146. The results are compared to

$^{13}\text{CO}$ ,  $\text{C}^{18}\text{O}$ , and CS molecular-line observations obtained at the same angular resolution. The primary results derived from our study can be summarized as follows.

1. We have constructed a detailed map of the distribution of extinction for the Northern Streamer cloud of the IC 5146 cloud complex at an effective spatial resolution of 1'.5. We have integrated this map to determine the total mass of the cloud and find a value of  $2800(D/1 \text{ kpc})^2$  with a statistical uncertainty of  $\pm 28 (D/1 \text{ kpc})^2 M_\odot$  for those regions where  $A_V$  is greater than 4 mag.

2. We find that the dispersion in our extinction measurements varies with derived mean extinction in an interesting and well-determined manner. In particular, the dispersion or error associated with an extinction determination appears to linearly increase with the derived mean extinction. In addition, the dispersion in the dispersion also increases with extinction. From analysis of the errors, modeling of the spatial distribution of extinction on small scales, and modeling the contribution of foreground stars, we find that variations in cloud structure on scales smaller than the resolution of our measurements dominate the observed errors at moderate and high extinctions in this cloud.

3. From our models, we demonstrate that the form of the observed  $\sigma_{\text{disp}}$  versus  $A_V$  relation can be used to place constraints on the nature of the spatial distribution of extinction on scales smaller than our resolution. In particular, we show that models in which the dust is distributed uniformly or in discrete high extinction clumps on scales smaller than 1'.5 are inconsistent with the observations.

4. We have derived extinctions at the same locations and at the same angular resolution (1'.7) as the  $^{13}\text{CO}$ ,  $\text{C}^{18}\text{O}$ , and CS observations we have obtained for this cloud. From comparison of the data we have determined the integrated intensity to  $A_V$  ratios for  $^{13}\text{CO}$ ,  $\text{C}^{18}\text{O}$ , and CS at higher angular resolution and to significantly deeper cloud depths ( $\approx 30$  visual magnitudes) than any previous study.

5. The integrated intensities of  $^{13}\text{CO}$ ,  $\text{C}^{18}\text{O}$ , and CS are found to be correlated with extinction. However, while the  $\text{C}^{18}\text{O}$  and CS emission appears to vary in a roughly linear manner over the entire range of measured extinction (i.e., 0–30 mag), the variation of  $^{13}\text{CO}$  emission with  $A_V$  is decidedly nonlinear. Our data clearly show that the  $^{13}\text{CO}$  emission saturates at cloud depths between 5–8 mag of visual extinction. This result has already been suggested in previous work performed at lower extinction ranges (e.g., Dickman 1978; Langer et al. 1989; Freking et al. 1982; Bachiller & Chernicaró 1986; Dickman & Herbst 1990).

6. There is a large scatter in all three correlations. The bulk of this scatter appears to be intrinsic and indicates that the abundances and/or excitation conditions for the molecules vary significantly from point to point in the cloud. This suggests that there is an intrinsic uncertainty (of a factor of 2–5 in magnitude) associated with determining cloud hydrogen abundances or masses from molecular-line observations.

7. The ratio of the of  $^{13}\text{CO}$  to  $\text{C}^{18}\text{O}$  LTE column densities varies with extinction. At extinctions below 10 mag, the ratio is significantly larger than the terrestrial value of 5.5, while it is very close to this value at larger cloud optical depths. More significantly, the dispersion in this column density ratio also varies with extinction and is very large for extinctions less than 10 mag. This suggests that the abundances of  $^{13}\text{CO}$  and  $\text{C}^{18}\text{O}$  are unstable down to cloud depths as deep as 10 mag. At the

highest extinctions the dispersion is quite small and the abundance of  $C^{18}O$  appears very stable.

8. From our observations we derive the following mean abundance ratios:  $2.18 \pm 0.24 \times 10^{15} \text{ cm}^{-2} \text{ mag}^{-1}$ ,  $2.29 \pm 0.72 \times 10^{14} \text{ cm}^{-2} \text{ mag}^{-1}$ , and  $4.5 \pm 0.9 \times 10^{11} \text{ cm}^{-2} \text{ mag}^{-1}$  for  $^{13}CO$ ,  $C^{18}O$ , and  $CS$ , respectively.

We thank John Black, Ned Ladd, Colin Masson, Lee Mundy, and Joao Yun for helpful discussions. This study was largely supported by NSF grant AST 8815753 awarded to the University of Arizona. Partial support was also provided by NASA grant NAG 5-1997 and NSF grants AST 8915606 and AST 9221194 awarded to Boston University.

#### REFERENCES

- Bachall, J., & Sonnerup, S. 1980, *ApJ*, 44, 73  
 Bachiller, T., & Cernicharo, J. 1986, *A&A*, 166, 283  
 Bally, J., Stark, A. A., Wilson, R. W., & Henkel, C. 1987, *ApJS*, 65, 113  
 Barnes, P., Myers, P. C., & Heyer, M. 1994, in preparation  
 Bessell, M. S., & Brett, J. M. 1988, *PASP*, 100, 1134  
 Bohlin, R. C., Savage, B. D., & Drake, J. F. 1978, *ApJ*, 224, 132  
 Bok, B. J. 1937, *The Distribution of Stars in Space* (Chicago: Univ. of Chicago Press)  
 Bok, B. J., & Cordwell, C. S. 1973, in *Molecules in the Galactic Environment*, ed. M. A. Gordon & L. E. Snyder (New York: Wiley), 53  
 Cernicharo, J., & Bachiller, R. 1984, *A&AS*, 58, 327  
 Dickman, R. L. 1978, *ApJS*, 37, 407  
 Dickman, R. L., & Herbst, W. 1990, *ApJ*, 357, 531  
 Dobashi, K., Yoonekura, Y., Mizuno, A., & Fukui, Y. 1992, *AJ*, 104, 1525  
 Duvert, G., Cernicharo, J., & Baudry, A. 1986, *A&A*, 164, 2  
 Elias, J. H. 1978, *ApJ*, 223, 859  
 Elias, J. H., Frogel, J. A., Matthews, K., & Neugebauer, G. 1982, *AJ*, 87, 1029  
 Frerking, M. A., Langer, W. D., & Wilson, R. W. 1982, *ApJ*, 262, 590  
 Henry, P. 1979, *Rev. Sci. Instr.*, 50, 185  
 Hyland, A. R. 1981, in *Infrared Astronomy*, ed. C. G. Wynn-Williams & D. P. Cruikshank (Dordrecht: Reidel), 125  
 Irvine, W. M., Goldsmith, P. F., & Hjalmarson, A. 1987, in *Interstellar Processes*, ed. D. J. Hollenbach & H. A. Thronson (Dordrecht: Reidel), 561  
 Jenkins, E. B., & Savage, D. B. 1974, *ApJ*, 187, 243  
 Jones, T. J., Hyland, A. R., & Bailey, J. A. 1981, *ApJ*, 282, 675  
 Koornneef, J. 1983, *A&A*, 128, 84  
 Lada, E. A., Lada, C. J., & Bally, J. 1994, in preparation  
 Lada, C. J., & Adams, F. C. 1992, *ApJ*, 393, 278  
 Lada, C. J., DePoy, D., Merrill, M., & Gatley, I. *ApJ*, 374, 533  
 Lada, C. J., & Elmegreen, B. G. 1978, *AJ*, 84, 336  
 Lada, C. J., Young, E. T., & Greene, T. P. 1993, *ApJ*, 408, 471  
 Langer, W. D., Wilson, R. W., Goldsmith, P. F., & Beichman, C. A. 1989, *ApJ*, 337, 355  
 Lilley, A. E. 1955, *ApJ*, 121, 559  
 Mathis, J. S. 1990, *ARA&A*, 28, 37  
 Mattila, K. 1986, *A&A*, 160, 157  
 Minn, Y. K., & Greenberg, J. M. 1979, *A&A*, 77, 37  
 Pound, M. W., Bania, T. M., & Wilson, R. W. 1990, *ApJ*, 351, 165  
 Rieke, G. H., & Lebofsky, M. J. 1985, *ApJ*, 288, 618  
 Rossano, G. S. 1980, *AJ*, 85, 1218  
 Sandell, G., Johansson, L. E. B., Nguyen-Q-Rieu, & Mattila, L. 1981, *A&A*, 97, 317  
 Savage, B. D., & Mathis, J. S. 1979, *ARA&A*, 17, 73  
 Straw, S. M., & Hyland, A. R. 1989, *ApJ*, 340, 318  
 Swade, D. 1989, *ApJ*, 345, 828  
 Swade, D., & Schloerb, P. F. 1992, *ApJ*, 392, 543  
 van Dishoeck, E., & Black, J. H. 1988, *ApJ*, 334, 771